Quantitative Evaluation of Enhanced Multi-plane Clinical Fetal Diffusion MRI with a Crossing-Fiber Phantom

Hamza Kebiri[1,2(✉)], Hélène Lajous[1,2], Yasser Alemán-Gómez[1], Gabriel Girard[3], Erick Canales Rodríguez[3], Sébastien Tourbier[1], Marco Pizzolato[3,4], Jean-Baptiste Ledoux[1,2], Eleonora Fornari[1,2], András Jakab[5,6], and Meritxell Bach Cuadra[1,2,3]

[1] Department of Radiology, Lausanne University Hospital and University of Lausanne, Lausanne, Switzerland
[2] CIBM Center for Biomedical Imaging, Lausanne, Switzerland
[3] Signal Processing Laboratory 5 (LTS5), Ecole Polytechnique Fédérale de Lausanne (EPFL), Lausanne, Switzerland
[4] Department of Applied Mathematics and Computer Science, Technical University of Denmark, Kgs. Lyngby, Denmark
[5] Center for MR Research, University Children's Hospital Zurich, Zurich, Switzerland
[6] Neuroscience Center Zurich, University of Zurich/ETH Zurich, Zurich, Switzerland

Abstract. Diffusion Magnetic Resonance Imaging (dMRI) has become widely used to study *in vivo* white matter tissue properties non-invasively. However, fetal dMRI is greatly limited in Signal-to-Noise ratio and spatial resolution. Due to the uncontrollable fetal motion, echo planar imaging acquisitions often result in highly degraded images, hence the ability to depict precise diffusion MR properties remains unknown. To the best of our knowledge, this is the first study to evaluate diffusion properties in a fetal customized crossing-fiber phantom. We assessed the effect of scanning settings on diffusion quantities in a phantom specifically designed to mimic typical values in the fetal brain. Orthogonal acquisitions based on clinical fetal brain schemes were preprocessed for denoising, bias field inhomogeneity and distortion correction. We estimated the fractional anisotropy (FA) and mean diffusivity (MD) from the diffusion tensor, and the fiber orientations from the fiber orientation distribution function. Quantitative evaluation was carried out on the number of diffusion gradient directions, different orthogonal acquisitions, and enhanced 4D volumes from scattered data interpolation of multiple series. We found out that while MD does not vary with the number of diffusion gradient directions nor the number of orthogonal series, FA is slightly more accurate with more directions. Additionally, errors in all scalar diffusion maps are reduced by using enhanced 4D volumes. Moreover, reduced fiber orientation estimation errors were obtained when used enhanced 4D volumes, but not with more diffusion gradient directions. From these results, we conclude that using enhanced 4D volumes from multiple series should be preferred over using more diffusion gradient directions in clinical fetal dMRI.

S. Cetin-Karayumak et al. (Eds.): CDMRI 2021, LNCS 13006, pp. 12–22, 2021.
https://doi.org/10.1007/978-3-030-87615-9_2

Keywords: Fetal · MRI · Brain · Phantom · Diffusion tensor imaging · Orientation distribution function · Scattered data interpolation

1 Introduction

Diffusion Magnetic Resonance Imaging (dMRI) has been the mainstay of non-invasive white matter investigation *in vivo*. As the diffusion signal is sensitive to the displacement of water molecules in brain tissues, various biophysical models have been proposed for estimating the underlying tissue architecture. These models can either be Gaussian, e.g., diffusion tensor imaging (DTI) is the most simple and widely used model to characterize the diffusion process, or non-Gaussian, e.g., q-ball imaging [31], diffusion spectrum imaging [2,34], and spherical deconvolution [3,30], which estimate Orientation Distribution Functions (ODFs) for resolving multiple intravoxel fiber orientations. However, the unavailability of a ground truth makes the quantitative validation of these models an elusive goal. Monkey brains have been used for connectivity validation of dMRI when compared to histological connectivity obtained from viral tracer injections [1]. Nevertheless, a direct comparison of diffusion orientations at the voxel level is challenging using orientations derived from histological data [27].

On the other hand, phantoms provide an additional possibility for the quantitative evaluation because they offer more controlled, reproducible, and easily accessible experiments. Physical phantoms have been used in dMRI validation setups. For example, the reproducibility of MD measurements was assessed in [17], whereas the recovery of the Ensemble average propagator was validated in a crossing phantom in [23]. In the Fiber Cup [5,10] and ISBI 2018 [26] challenges, tractography reconstructions were compared to ground-truth fiber configurations from physical phantoms. Synthetic software-based phantoms also proved to be a valid alternative to physical phantoms for validation purposes, e.g., see [21,24] and references therein.

In fact, fetal subjects are a sensitive cohort, thus preventing from assessing different acquisition configurations. Hence, the evaluation of our technique on a quantitative dMRI phantom is crucial before applying it to *in vivo* data. However, designing a phantom that matches a fetal brain is extremely complex and challenging. In this work, we use a small size phantom with a customized fractional anisotropy (FA) in the single fiber population in the upper values reported in fetal brains. Indeed, in their atlas, Khan et al. [15] modelled the splenium of the corpus callosum (CC) of a fetus of 37 gestational weeks with an approximately close FA. Similar values were reported both for the genu and the splenium of the CC [8]. Therefore, our phantom is relevant to perform a benchmark analysis in fetuses in the 3rd trimester of gestation. Additionally, the dMRI signal obtained from physical phantoms is similar to *in vivo* data and is more realistic than the dMRI signal obtained from numerical simulations.

Fetal dMRI severely suffers from the unpredictable motion and artifacts caused by the small fetal brain structure that is surrounded by amniotic fluid

and maternal organs. Scanning times are typically shorter than that of post-natal studies, limiting the possibility of long diffusion MRI acquisitions based on a large number of diffusion gradient directions and high b-values, which are required to disentangle complex fiber configurations. Furthermore, the use of fast Echo Planar Imaging acquisitions to freeze intra-slice motion leads to highly blurred and distorted images. These images also have a low Signal-to-Noise ratio (SNR), due to the tissue properties of the fetal white matter. Orthogonal scans of anisotropic resolution are usually acquired to overcome these pitfalls. In clinical practice, there is a strong constraint on scanning time, often below 10 min. This does not allow to acquire a high number of orthogonal volumes and a high number of diffusion directions at the same time. Additionally, clinical protocols are not consensual between sites. Typically, clinical fetal brain dMRI have an in-plane resolution of 1–2 mm, a slice thickness of 3–5 mm, the number of gradient directions ranges between 4 and 32, and unique b-values between 400 and 1000 s/mm^2 are employed [12,19,20]. Conversely, in the pioneer research initiative of Developing Human Connectome Project protocol (DHCP) [4,6], up to 141 diffusion volumes can be acquired with multiple b-values (400 and 1000 s/mm^2) and a scanning time of about 15 min per 4D volume.

Our study focuses on the quantitative evaluation of the accuracy of DTI and ODF reconstructions from *in vivo* fetal dMRI acquisitions to identify a good trade-off between the number of series and the number of diffusion gradient directions in a more clinically realistic scenario (summarized in Fig. 1).

2 Methodology

2.1 Materials

Fetal Crossing Phantom - We used a customized fiber crossing phantom (diameter & height of 150 mm) [22] made of two interleaved polyester fiber strands encapsulated in an aqueous solution. The fibers diameter is of 15 µm, the crossing angle between the two strands is approximately 60°, and a customized FA to mimic fetal values in the single fiber population of 0.6 was requested. These values were reported by the vendor who computed them from 128 diffusion-weighted images (DWI) and $b = 1000$ s/mm^2. (Fig. 1A).

MRI Acquisitions - High-resolution (HR) (spatial and angular) images were acquired at 3T (MAGNETOM Prisma-Fit, Siemens Healthcare, Erlangen, Germany), with a 16-channel body array coil and a 32-channel spine coil using a pulsed gradient spin-echo (PGSE) sequence with four different b-values, $400, 700, 1000$ and 3000 s/mm^2. The spatial resolution was 1.5 mm^3 isotropic with a field of view of $256 \times 256 \times 88$ mm^3 , acquired with 61 directions. The echo time (TE) was 52 ms, the repetition time (TR) was 4200 ms and the flip angle was 90°. Only the $b = 700$ s/mm^2 acquisition was considered as the pseudo ground truth (pseudo-GT) in the validation framework.

Low-resolution (LR) acquisitions were performed at 1.5T (MAGNETOM Sola, Siemens Healthcare, Erlangen, Germany), with an 18-channel body array

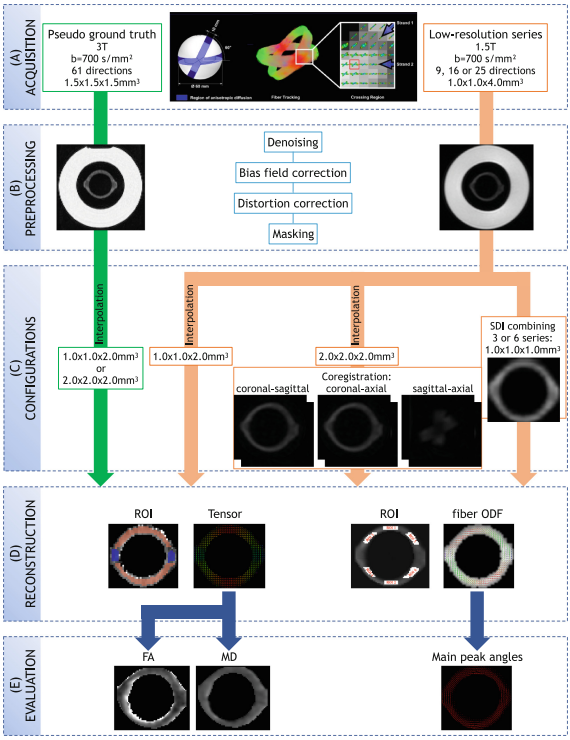

Fig. 1. Summary of our phantom evaluation framework for fetal dMRI acquisitions.

coil and a 32-channel spine coil, using a PGSE sequence (TE = 82 ms, TR = 2000 ms, flip angle = 90°). The acquisition time was approximately one minute per 4D volume. The in-plane resolution was 1×1 mm^2, the slice thickness was 4 mm and the field of view $207 \times 207 \times 69$ mm^3. We used $b = 700$ s/mm^2 and either 9, 16 or 25 directions, uniformly distributed in the half-sphere. In order to correct non-linear distortions, we also acquired a 1 mm isotropic T2-weighted (T2-w) image using a Sampling Perfection with Application optimized Contrasts using different flip angle Evolution (SPACE) sequence (TE = 380 ms, TR = 3200 ms). Both our data[1] and code[2] will be available to ensure reproducibility of the results.

2.2 Data Processing

Preprocessing - Both the pseudo-GT and LR datasets were preprocessed as follows: a denoising step using a Principal Component Analysis based method

[1] www.zenodo.org/record/5153507#.YQgEA3UzbRY.
[2] www.github.com/Medical-Image-Analysis-Laboratory/FetalBrainDMRI_CrossingPhantom.

[33], followed by an N4 bias-field inhomogeneity correction [32]. Distortion was corrected using a state-of-the-art algorithm for fetal brain [16]. We started by a rigid registration of the distortion free T2-w image to the b0 (b =0 s/mm^2) image followed by a non-linear registration in the phase-encoding direction of the b0 to the same T2-w image. The transformation was then applied to the diffusion-weighted images.

Definition of Regions-of-Interest (ROI) - Masks of the fiber endpoint regions (single fiber and crossing fiber ROIs) were obtained using mathematical morphology operations, intensity thresholding in the b0 image and manual refinement. Manual segmentation of each region was performed in the $1 \times 1 \times 2$ mm^3 resolution and propagated by nearest neighbor interpolation and manual refinement to other resolution volumes. Borders were not considered to avoid partial volume effect. The single fiber ROI was further subdivided in six ROIs: ROI 1 and ROI 2 in which the fibers are oriented horizontally and ROI 3–6 where they are oblique (Fig. 1D).

Interpolation - Since the pseudo-GT and LR series have very different resolutions, they were both mapped to a middle ground resolution of $1 \times 1 \times 2$ mm^3 and $2 \times 2 \times 2$ mm^3 using trilinear interpolation. We chose these trade-off resolutions to avoid to significantly degrade the pseudo-GT by introducing artifacts and to enhance the LR volumes as it was demonstrated in [7]. Additionally, upsampling LR DWI images by a factor of two is a common practice in clinical fetal dMRI [13]. The $1 \times 1 \times 2$ mm^3 resolution was used for unique volumes, i.e., either axial, coronal or sagittal and the $2 \times 2 \times 2$ mm^3 resolution for combined ones, i.e., axial-coronal, axial-sagittal or coronal-sagittal. For the combined volumes, we registered the b0 images of the coronal and the sagittal acquisitions to the b0 image of the axial one using landmarks [9]. This transformation was then applied to the DWI images. To reduce error propagation related to interpolation, we have performed the latter after the preprocessing. We have also computed the different metrics at the different resolutions to quantify variations linked to interpolating the data.

Scattered Data Interpolation - We generated a HR volume from a set of either three or six LR orthogonal series using Scattered Data Interpolation (SDI) reconstruction [25] as implemented in MIALSRTK (version 2.0.1) [28]. It was applied separately to each DWI image and each b0. This consisted in coregistering to an axial reference volume, resampled to isotropic high-resolution, all the series as a first step. Then, the intensity of each voxel in the HR volume grid was computed by averaging the intensities of the corresponding neighboring voxels in the LR volumes using a Gaussian kernel. To match the underlying point spread function of the data, the Gaussian kernel profile was set to be perpendicular to the slice plane with a zero mean and a Full Width at Half Maximum (FWHM of $\sim$2.355 standard deviation) equal to the voxel resolution.

Reconstruction - We reconstructed (1) the diffusion tensor from which we derived both the FA and mean diffusivity (MD) maps and (2) the fiber ODF using the constrained spherical deconvolution (CSD) method [30] from which the

main peak (i.e., fiber orientation) was determined. The fiber ODF is represent ed in the Spherical Harmonics (SH) basis, where an order 4 (15 parameters) was used to best fit all directions (15, 25 for the LR volumes and 61 for the pseudo-GT) and be able to make a one-to-one comparison. In the CSD algorithm, we have constrained the maximum number of peaks to two and the minimum separation angle to 25°. Dipy (version 1.3.0) [11] was used for reconstruction and visualization, and MRtrix3 [29] for fiber ODF visualization.

Evaluation Metrics - To be able to fairly compare diffusion metrics, unbiased by different b-values, we only used as reference the HR data acquired with the same b-value i.e. $b = 700$ s/mm^2 (i.e., pseudo-GT) as the LR data. Scalar maps were evaluated by computing the relative difference between images, i.e., difference between the average LR and the average pseudo-GT map, divided by the average pseudo-GT map. The coefficient of variation (CV, i.e., standard deviation/mean) was also used to quantify the variability of scalar maps.

3 Results

3.1 Scalar Maps

Evaluation of Pseudo-GT - We first assessed the pseudo-GT compared to the diffusion properties given by the vendor. The estimated FA from the pseudo-GT was found to be equal to 0.367 (horizontal orange line in Fig. 2) which did not correspond to the FA reported by the vendor (0.6) in the single fiber population. This is not surprising since FA strongly depends on the acquisition parameters, and in particular on the b-value. Indeed, the same observation was made in the Fiber Cup study [10], where an increase of 75% in the mean FA was reported between $b = 650$ s/mm^2 and $b = 2000$ s/mm^2. The computed FA of 0.367 falls in the same range of FA reported in [14] (using $b = 700$ s/mm^2 & 32 directions) for various fetal brain structures. Conversely, the mean MD = 1.165 mm^2/s was more consistent with the value reported by the vendor (i.e., $\sim$1.2 mm^2/s).

Let us note that scalar maps did not show major differences across different pseudo-GT interpolations, with a CV of 0.5% for single fiber and up to 6.5% for crossing populations. This is lower than the CV of the FA (up to 22%) and MD (up to 12%) values within single and crossing fibers areas of each scalar maps.

Assessment of Enhanced Acquisitions - Figure 2 shows the results from the LR scalar maps for the different configurations compared to the pseudo-GT (two horizontal lines). The orange color refers to the single fiber population and the blue color to the crossing fiber populations, and the bigger the disk diameter the more diffusion directions are used in the reconstruction. For FA, SDI methods outperform the other configurations, especially when considering the single fiber population that shows a difference from the pseudo-GT of 6.1%. Single LR volumes and combinations of pairs are more sensitive to the number of diffusion directions (in these cases, the more directions, the smaller the error), whereas SDI does not show this influence.

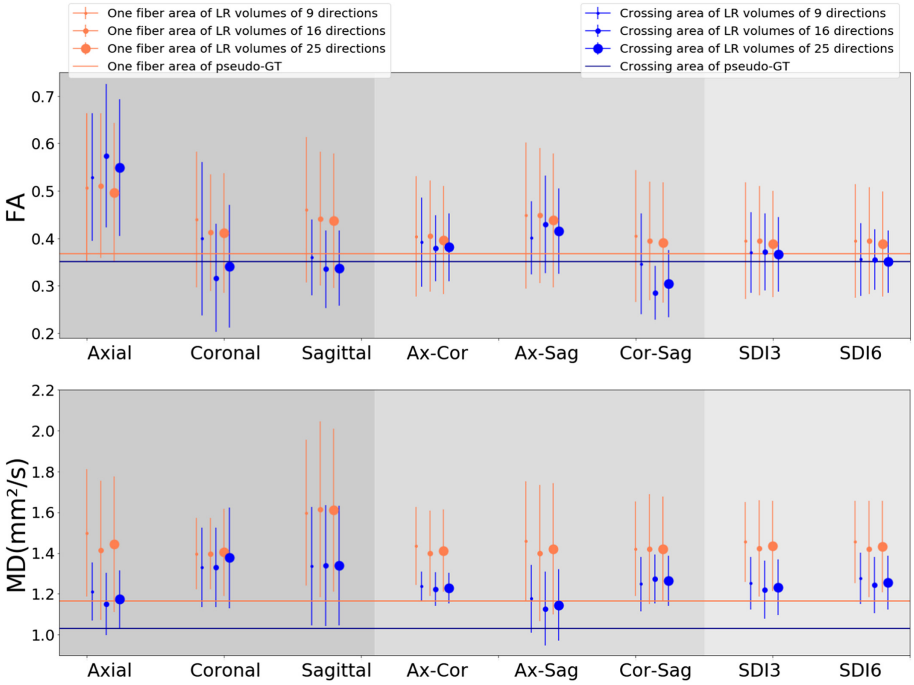

Fig. 2. Scalar maps estimation error compared to the pseudo-GT (horizontal lines, single fiber in orange, crossings in blue, see Fig. 1D). Axial, Coronal, and Sagittal data correspond to single volumes with a resolution of $1 \times 1 \times 2$ mm^3. Ax-Cor, Ax-Sag, and Cor-Sag denote combined volumes with a resolution of 2 mm isotropic. SDI3 and SDI6 are the interpolated scattered data by using three or six 1 mm isotropic volumes, respectively. (Color figure online)

The axial acquisition exhibits a singular behaviour compared to the two other single-volume acquisitions, depicting a higher FA in the crossing area compared to the single fiber area. By inspecting the scanner FA map, we found out an already high FA, particularly in the crossing area of 17% more than in the coronal and the sagittal maps. So merging orthogonal volumes can reduce any potential discrepancy between the different acquisitions (due to outliers and artifacts in the data or due to the anisotropy of the acquisitions capturing the non-symmetrical anatomy across planes of the fibers) and SDI provides the most robust solution.

Differently than FA, MD errors are not influenced by the number of directions neither for single, pairs nor SDI volumes. Both merging pairs of orthogonal volumes and SDI reconstructions help attenuate the high error rate of the sagittal volume by a difference from the average pseudo-GT of about 15% (single fiber population) and 20% (crossing area). The difference between the LR and pseudo-GT values can be explained by the magnetic field strength. Indeed, it was shown in [18], that MD was significantly different between 1.5T and 3T acquisitions.

3.2 Fiber Orientation Errors

Fiber orientations estimation in the pseudo-GT across interpolations is stable in the different ROIs. The maximum standard deviation in ROIs 1–2, where the fibers are close to the x-axis coordinates, is 1.6°, whereas it reaches 4.5° in ROIs 3–6 where the fibers are rotated by around 50°. As depicted in Fig. 3, the angular error of the LR estimated orientations doesn't correlate to the different orthogonal volumes configurations, except for SDI that always shows a lower angular error than, at least, the most under-performing single volume reconstruction. Furthermore, we can observe that the standard deviation of the angular error (vertical lines in Fig. 3) strongly depends on the region of interest. For instance, ROI 1 angles are less variant and closer to the pseudo-GT whereas in ROI 2, the sagittal acquisition compromises the estimated angle of other reconstructions where it belongs. In contrast to ROI 4 and ROI 6, the errors in ROI 3 and ROI 5 are not dramatic as they are located below the mean separation angle of 25°. Importantly, the error difference between the LR and the pseudo-GT volumes is independent of the number of diffusion directions used to compute the main ODF peak.

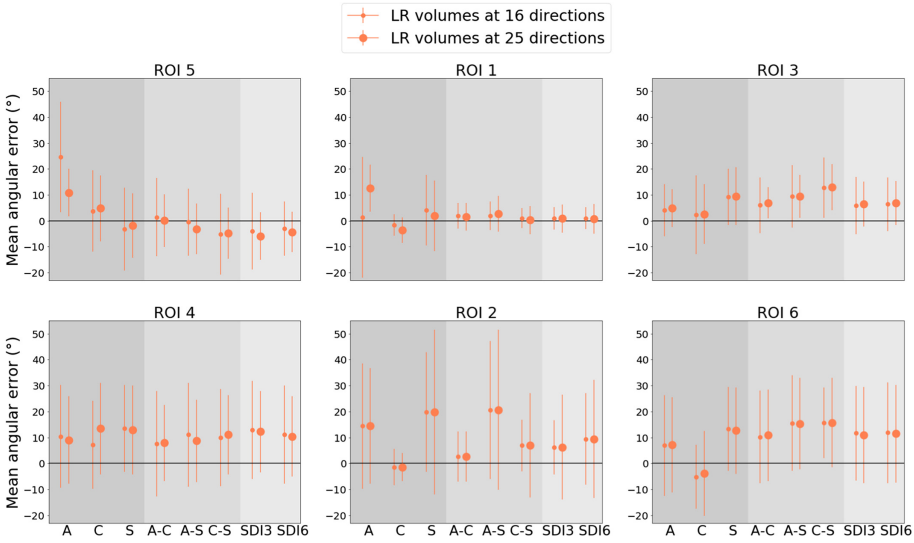

Fig. 3. Mean angular error in different single fiber ROIs corresponding to Fig. 1D for different configurations. Graphs for each ROI are positioned in the corresponding order of their locations on the phantom. A: Axial, C: Coronal, S: Sagittal.

Figure 4A shows fiber ODFs overlaid on the FA map of a LR volume. As can be noted, only very few crossing fibers can be detected at $b = 700$ s/mm^2.

Results shown in Fig. 4B demonstrated that in the HR data, fiber crossings (i.e., two peaks) can only be significantly resolved at $b = 3000$ s/mm^2. In the

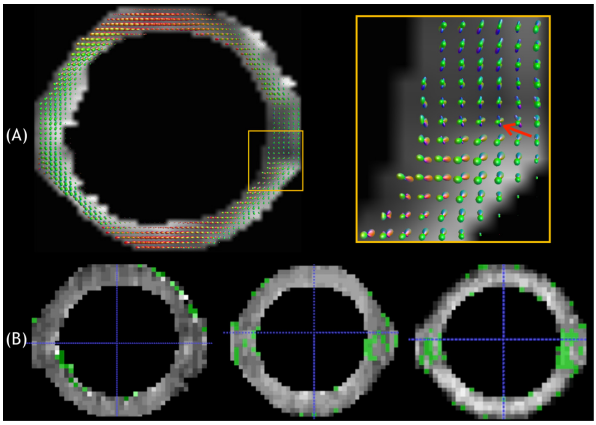

Fig. 4. (A) Fiber ODFs of a LR coronal image overlaid on the FA map. Red arrow: detected crossing. (B) Voxels detected as two peaks in the high resolution acquisition using b-values of 700, 1000 and 3000 s/mm^2 (left to right, respectively). (Color figure online)

crossing region, a median inter-fiber angle of 62° close to that reported by the vendor (i.e., 60°) was detected by using a SH order of 8, although with a high standard deviation of 29°. For this reason, we did not perform fiber orientation analyses in the fiber crossing area of the LR data.

4 Conclusion and Discussion

We have demonstrated how reported diffusion properties of a fetal customized crossing phantom vary across orthogonal series and the number of diffusion directions, and how scattered data interpolation of multiple volumes can reduce this variability and so better approximate the pseudo ground truth. Increasing the number of directions did not consistently reduce error metrics (MD, FA, and fiber orientations) because of the low b-value and the relatively low number of directions employed, which only allow estimating a single fiber per voxel. The main limitation of this study is the absence of unpredictable motion which is one of the main challenges in fetal MRI. However, random motion could be a confounding factor to evaluate different acquisition schemes. Hence setting up a first ideal motion-free scenario to quantify the maximum expected variability of fetal dMRI measurements is a key starting point. Hence, these conclusions have to be taken as an upper bound that can be achieved. In future studies, we plan to extend this work by considering other acquisition protocols (such as the DHCP protocol), by using motion-induced acquisitions for testing different super-resolution reconstruction methods [6], and by implementing scan-rescan analyses in different scanners.

Acknowledgments. This work was supported by the Swiss National Science Foundation (project 205321-182602, grant No 185897: NCCR-SYNAPSY- "The synaptic bases of mental diseases" and the Ambizione grant PZ00P2_185814), the Centre d'Imagerie BioMédicale (CIBM) of the University of Lausanne (UNIL), the Swiss Federal Institute of Technology Lausanne (EPFL), the University of Geneva (UniGe), the Centre Hospitalier Universitaire Vaudois (CHUV), the Hôpitaux Universitaires de Genève (HUG), and the Leenaards and Jeantet Foundations. This work was also supported by the European Union's Horizon 2020 research and innovation programme under the Marie Skłodowska-Curie grant agreement No 754462.

References

1. Aydogan, D.B., et al.: When tractography meets tracer injections: a systematic study of trends and variation sources of diffusion-based connectivity. Brain Struct. Funct. **223**(6), 2841–2858 (2018)
2. Canales-Rodríguez, E.J., Iturria-Medina, Y., Alemán-Gómez, Y., Melie-García, L.: Deconvolution in diffusion spectrum imaging. Neuroimage **50**(1), 136–149 (2010)
3. Canales-Rodríguez, E.J., Legarreta, J.H., Pizzolato, M., Rensonnet, G., Girard, G., Patino, J.R., et al.: Sparse wars: a survey and comparative study of spherical deconvolution algorithms for diffusion MRI. NeuroImage **184**, 140–160 (2019)
4. Christiaens, D., et al.: Fetal diffusion mri acquisition and analysis in the developing human connectome project. In: Proceedings of the Annual Meeting of the International Society of Magnetic Resonance in Medicine (ISMRM) (2019)
5. Côté, M.A., Girard, G., Boré, A., Garyfallidis, E., Houde, J.C., Descoteaux, M.: Tractometer: Towards validation of tractography pipelines. Med. Image Anal. **17**(7), 844–857 (2013)
6. Deprez, M., Price, A., Christiaens, D., Estrin, G.L., Cordero-Grande, L., et al.: Higher order spherical harmonics reconstruction of fetal diffusion mri with intensity correction. IEEE Trans. Med. Imaging **39**(4), 1104–1113 (2019)
7. Dyrby, T.B., et al.: Interpolation of diffusion weighted imaging datasets. NeuroImage **103**, 202–213 (2014)
8. Estrin, G.L., et al.: White and grey matter development in utero assessed using motion-corrected diffusion tensor imaging and its comparison to ex utero measures. Magn. Reson. Mater. Phys. Biol. Med. **32**(4), 473–485 (2019)
9. Fedorov, A., Beichel, R., Kalpathy-Cramer, J., Finet, J., et al.: 3d slicer as an image computing platform for the quantitative imaging network. Magn. Reson. Imaging **30**(9), 1323–1341 (2012)
10. Fillard, P., Descoteaux, M., Goh, A., Gouttard, S., Jeurissen, B., et al.: Quantitative evaluation of 10 tractography algorithms on a realistic diffusion MR phantom. NeuroImage **56**(1), 220–234 (2011)
11. Garyfallidis, E., et al.: Dipy, a library for the analysis of diffusion MRI data. Front. Neuroinf. **8** (2014). https://doi.org/10.3389/fninf.2014.00008
12. Jakab, A., et al.: Disrupted developmental organization of the structural connectome in fetuses with corpus callosum agenesis. Neuroimage **111**, 277–288 (2015)
13. Jakab, A., Tuura, R., Kellenberger, C., Scheer, I.: In utero diffusion tensor imaging of the fetal brain: a reproducibility study. NeuroImage: Clin. **15**, 601–612 (2017)
14. Kasprian, G., et al.: In utero tractography of fetal white matter development. Neuroimage **43**(2), 213–224 (2008)
15. Khan, S., et al.: Fetal brain growth portrayed by a spatiotemporal diffusion tensor MRI atlas computed from in utero images. NeuroImage **185**, 593–608 (2019)

16. Kuklisova-Murgasova, M., et al..: Distortion correction in fetal epi using non-rigid registration with a laplacian constraint. IEEE Trans. Med. Imaging **37**(1) (2017). https://doi.org/10.1109/ISBI.2016.7493522
17. Lavdas, I., Behan, K.C., Papadaki, A., McRobbie, D.W., Aboagye, E.O.: A phantom for diffusion-weighted MRI (DW-MRI). J. Magn. Reson. Imaging **38**(1), 173–179 (2013)
18. Lavdas, I., Miquel, M.E., McRobbie, D.W., Aboagye, E.O.: Comparison between diffusion-weighted MRI (DW-MRI) at 1.5 and 3 tesla: a phantom study. J. Magn. Reson. Imaging **40**(3), 682–690 (2014)
19. Machado-Rivas, F., et al.: Tractography of the cerebellar peduncles in second-and third-trimester fetuses. Am. J. Neuroradiol. **42**(1), 194–200 (2021)
20. Machado-Rivas, F., et al.: Spatiotemporal changes in diffusivity and anisotropy in fetal brain tractography (2021)
21. Maier-Hein, K.H., et al.: The challenge of mapping the human connectome based on diffusion tractography. Nature Commun. **8**(1) (2017)
22. Moussavi-Biugui, A., Stieltjes, B., et al.: Novel spherical phantoms for q-ball imaging under in vivo conditions. Magn. Reson. Med. **65**(1), 190–194 (2011)
23. Ning, L., Laun, F., Gur, Y., DiBella, E.V., Deslauriers-Gauthier, S., Megherbi, T., et al.: Sparse Reconstruction Challenge for diffusion MRI: validation on a physical phantom to determine which acquisition scheme and analysis method to use? Med. Image Anal. **26**(1), 316–331 (2015)
24. Rafael-Patino, J., Romascano, D., Ramirez-Manzanares, A., Canales-Rodríguez, E.J., Girard, G., Thiran, J.P.: Robust Monte-Carlo Simulations in Diffusion-MRI: Effect of the substrate complexity and parameter choice on the reproducibility of results (2019)
25. Rousseau, F., et al.: Registration-based approach for reconstruction of high-resolution in utero fetal MR brain images. Acad. Radiol. **13**(9), 1072–1081 (2006)
26. Schilling, K.G., Gao, Y., Stepniewska, I., Janve, V., Landman, B.A., Anderson, A.W.: Anatomical accuracy of standard-practice tractography algorithms in the motor system - a histological validation in the squirrel monkey brain. Magn. Reson. Imaging **55**, 7–25 (2019)
27. Schilling, K.G., Janve, V., Gao, Y., Stepniewska, I., Landman, B.A., Anderson, A.W.: Histological validation of diffusion MRI fiber orientation distributions and dispersion. NeuroImage **165**, 200–221 (2018)
28. Tourbier, S., Bresson, X., Hagmann, P., Thiran, J.P., Meuli, R., Cuadra, M.B.: An efficient total variation algorithm for super-resolution in fetal brain MRI with adaptive regularization. NeuroImage **118**, 584–597 (2015)
29. Tournier, J.D., Smith, R., Raffelt, D., Tabbara, R., Dhollander, T., et al.: MRtrix3: a fast, flexible and open software framework for medical image processing and visualisation. NeuroImage **202**, 116137 (2019)
30. Tournier, J.D., Yeh, C.H., Calamante, F., Cho, K.H., Connelly, A., Lin, C.P.: Resolving crossing fibres using constrained spherical deconvolution: validation using diffusion-weighted imaging phantom data. Neuroimage **42**(2), 617–625 (2008)
31. Tuch, D.S.: Q-ball imaging. Magn. Reson. Med.: Off. J. Int. Soc. Magn. Reson. Med. **52**(6), 1358–1372 (2004)
32. Tustison, N.J., Avants, B.B., Cook, P.A., Zheng, Y., et al.: N4itk: improved n3 bias correction. IEEE Trans. Med. Imaging **29**(6), 1310–1320 (2010)
33. Veraart, J., Fieremans, E., Novikov, D.S.: Diffusion MRI noise mapping using random matrix theory. Magn. Reson. Med. **76**(5), 1582–1593 (2016)
34. Wedeen, V.J., et al.: Diffusion spectrum magnetic resonance imaging (DSI) tractography of crossing fibers. Neuroimage **41**(4), 1267–1277 (2008)